remote sensing

MDPI

Article

Activation of Ms 6.9 Milin Earthquake on Sedongpu Disaster Chain, China with Multi-Temporal Optical Images

Yubin Xin [1], Chaoying Zhao [1,2,3,4], Bin Li [2,*], Xiaojie Liu [5], Yang Gao [2] and Jianqi Lou [1]

[1] School of Geological Engineering and Geomatics, Chang'an University, Xi'an 710054, China; 2022226015@chd.edu.cn (Y.X.); cyzhao@chd.edu.cn (C.Z.); 2022026020@chd.edu.cn (J.L.)
[2] Institute of Geomechanics, Chinese Academy of Geological Sciences, Beijing 100081, China; gaoy@mail.cgs.gov.cn
[3] Key Laboratory of Western China's Mineral Resources and Geological Engineering, Ministry of Education, Xi'an 710054, China
[4] Key Laboratory of Ecological Geology and Disaster Prevention, Ministry of Natural Resources, Xi'an 710054, China
[5] School of Civil Engineering in Surveying and Mapping, Lanzhou University of Technology, Lanzhou 730050, China; xiaojieliu@chd.edu.cn
* Correspondence: lib_lxs@mail.cgs.gov.cn

Abstract: In recent years, disaster chains caused by glacier movements have occurred frequently in the lower Yarlung Tsangpo River in southwest China. However, it is still unclear whether earthquakes significantly contribute to glacier movements and disaster chains. In addition, it is difficult to measure the high-frequency and large gradient displacement time series with optical remote sensing images due to cloud coverage. To this end, we take the Sedongpu disaster chain as an example, where the Milin earthquake, with an epicenter 11 km away, occurred on 18 November 2017. Firstly, to deal with the cloud coverage problem for single optical remote sensing analysis, we employed multiple platform optical images and conducted a cross-platform correlation technique to invert the two-dimensional displacement rate and the cumulative displacement time series of the Sedongpu glacier. To reveal the correlation between earthquakes and disaster chains, we divided the optical images into three classes according to the Milin earthquake event. Lastly, to increase the accuracy and reliability, we propose two strategies for displacement monitoring, that is, a four-quadrant block registration strategy and a multi-window fusion strategy. Results show that the RMSE reduction percentage of the proposed registration method reaches 80%, and the fusion method can retrieve the large magnitude displacements and complete displacement field. Secondly, the Milin earthquake accelerated the Sedongpu glacier movement, where the pre-seismic velocities were less than 0.5 m/day, the co-seismic velocities increased to 1 to 6 m/day, and the post-seismic velocities decreased to 0.5 to 3 m/day. Lastly, the earthquake had a triggering effect around 33 days on the Sedongpu disaster chain event on 21 December 2017. The failure pattern can be summarized as ice and rock collapse in the source area, large magnitude glacier displacement in the moraine area, and a large volume of sediment in the deposition area, causing a river blockage.

Keywords: cross-platform optical image correlation; Sedongpu basin; glacier displacement; Milin earthquake; disaster chain

check for updates

Citation: Xin, Y.; Zhao, C.; Li, B.; Liu, X.; Gao, Y.; Lou, J. Activation of Ms 6.9 Milin Earthquake on Sedongpu Disaster Chain, China with Multi-Temporal Optical Images. *Remote Sens.* **2024**, *16*, 4003. https://doi.org/10.3390/rs16214003

Academic Editor: Matteo Albano

Received: 31 August 2024
Revised: 24 October 2024
Accepted: 25 October 2024
Published: 28 October 2024

Copyright: © 2024 by the authors. Licensee MDPI, Basel, Switzerland. This article is an open access article distributed under the terms and conditions of the Creative Commons Attribution (CC BY) license (https://creativecommons.org/licenses/by/4.0/).

1. Introduction

In the context of global warming, most glaciers are experiencing substantial melting and transformation, particularly in western China, which has led to an increased frequency of ice-rock avalanches [1–4]. The lower Yarlung Tsangpo River region, influenced by tectonic, geological, and seismic factors, is one of the most avalanche-prone areas in the world [5–9]. Disasters initiated by glacier ablation often do not manifest as isolated collapses or landslides. Instead, they develop into complex disaster chains that include

ice-rock avalanches, debris flows, dammed lakes, and flood outbursts. These events pose great threats to lives, properties, and major infrastructure projects [10], as evidenced by the Zelongnong landslides in 1950 and 1969 [11,12], the Yigong debris avalanche in 2000 [13,14], and the Uttarakhand ice and rock avalanche in 2021 [15,16]. Global attention on these disaster chains highlights their complexity and the challenges associated with their remote high mountain valleys, making it difficult to be identified and monitored [17–21].

The Sedongpu basin, situated in the lower reaches of the Yarlung Tsangpo River, has experienced dozens of ice-rock avalanche disaster chains since the 1950s. Following the Ms 6.9 Milin earthquake on 18 November 2017, another ice-rock avalanche disaster occurred about one month later on 21 December 2017 [22–25]. Glacier ablation, contributing to decreased glacier stability and more frequent glacier movements, poses a substantial threat to human lives and regional development [26]. These disaster chains have potential impacts on the safety of large-scale hydropower stations and the socio-economic development of local areas. Therefore, it is important to identify and monitor the early-stage glacier movements in the Sedongpu region and to analyze the correlation with the Milin earthquake.

However, it is still challenging to monitor the glacier displacement with in situ equipment, which is hard to install. Spaceborne and airborne remote sensing images provide valuable observations [27]. In particular, the image correlation to optical images demonstrates potential ability. The image cross-correlation for optical images can estimate pixel offsets of ground feature points, enabling high-precision monitoring of large gradient displacement [28,29]. This approach offers three advantages in quantitative displacement monitoring, including (1) steep slopes with close-to-nadir geometry observation; (2) north–south displacements; and (3) over dense vegetation area and over long temporal spanning. Numerous researchers utilize single-sensor or multiple-sensor observations to quantify the displacement of disaster events [30–32]. For instance, in 2018, Stumpf et al. investigated the time series displacement acceleration phenomenon of landslides by co-registration of Landsat-8 and Sentinel-2 images using Coregis software 2018 [33]. In 2020, Ding et al. employed optical image correlation techniques to fuse displacement from Landsat-8, Sentinel-2, and Gaofen-2 images to study the precursory displacement of landslide damages in Baige on 11 October and 3 November 2018 [34]. In 2023, Ding et al. derived the time series displacement of Sedongpu Glacier at different stages using Landsat-8 and Sentinel-2 images, finding rapid changes as a key factor for early warning of potential ice avalanche disasters [35]. Yang et al. fused Sentinel-1 and Landsat-8 data to monitor 3D motion of the Shishapangma Peak glacier based on variance component estimation, and the accuracies in the north–south and east–west directions were improved by 38% and 8%, respectively [36]. Zhao et al. used the Helmert variance component estimation method for SAR and optical offset tracking results to obtain the three-dimensional displacement of the Jianshanying landslide in Guizhou Province, China [37]. In 2024, Li et al. studied the formation mechanism of the Sedongpu disaster chain that occurred in October 2018, where a retrospective analysis was conducted on the formation conditions, evolution processes, and specific kinematic processes [38]. Generally, previous studies process optical images with the platforms and only fuse results from different platforms to estimate the displacement time series. Some images cannot be used due to their long temporal baseline relative to the specific event, like earthquakes or heavy rainfall, which makes it impossible to analyze the correlation between influencing factors and disaster chains in remote mountainous areas. Therefore, this study proposes a cross-platform image correlation technique to fuse the optical images from different platforms to obtain the high temporal displacement time series, where a four-quadrant block registration strategy is proposed to eliminate the systematic errors and a multi-window fusion strategy is adopted to suppress the gross error. To reveal the correlation between earthquake and disaster chain, we calculate the glacier displacement in three stages: pre-seismic, co-seismic, and post-seismic. Finally, we jointly analyze the glacier displacement time series, the Milin earthquake on 18 November 2017, and the Sedongpu disaster event on 21 December 2017.

2. Study Area and Datasets

2.1. Study Area

As shown in Figure 1, the Sedongpu Basin is located on the western slope of Gyala Peri Peak, on the left bank of the Yarlung Zangbo River in Milin County, Tibet, China. Covering an area of approximately 66.89 km^2, it falls within the plateau temperate semi-humid monsoon climate zone, with an average annual temperature of 8.2 °C and an average annual precipitation of 600 mm. About 85% of the rainfall is concentrated from June to September, and a frost-free period lasts around 170 days. The highest elevation in the study area is 7294 m at the summit of Gyala Peri Peak, whereas the lowest one is 2746 m at the inlet of the Sedongpu into the Yarlung Zangbo River, resulting in an elevation difference of 4548 m. Geomorphologically, the area lies at the juncture of the majestic Himalayas, the Nyingchi Tanggula Range, and the Hengduan Mountains, featuring deep river valleys and typical alpine valley morphologies. It represents a terrain within the Tibetan Plateau characterized by the most intense uplift and erosion processes. Tectonically, it is positioned at the easternmost extremity of the Himalayan Syntaxis, resulting from the tectonic collision between the Indian and Eurasian plates, constituting a zone characterized by intense tectonic activities, including extrusion, rotational fault, and significant uplift. The lithology strata comprise the gneiss and metavolcanic Namjbarwa Group marble, which have been eroded by glacial processes and physical weathering. The Sedongpu basin is surrounded by several faults, where the Chayu earthquake occurred in 1950 with Ms 8.6, and the Milin earthquake occurred in 2017 with Ms 6.9 [39]. This basin is prone to disaster chain events, including ice avalanches, rock avalanches, landslides, debris flows, and river blockages, which result in the accumulation and congestion of the Yarlung Zangbo River channel, posing a threat to downstream areas and obstructing the normal execution of major projects [40].

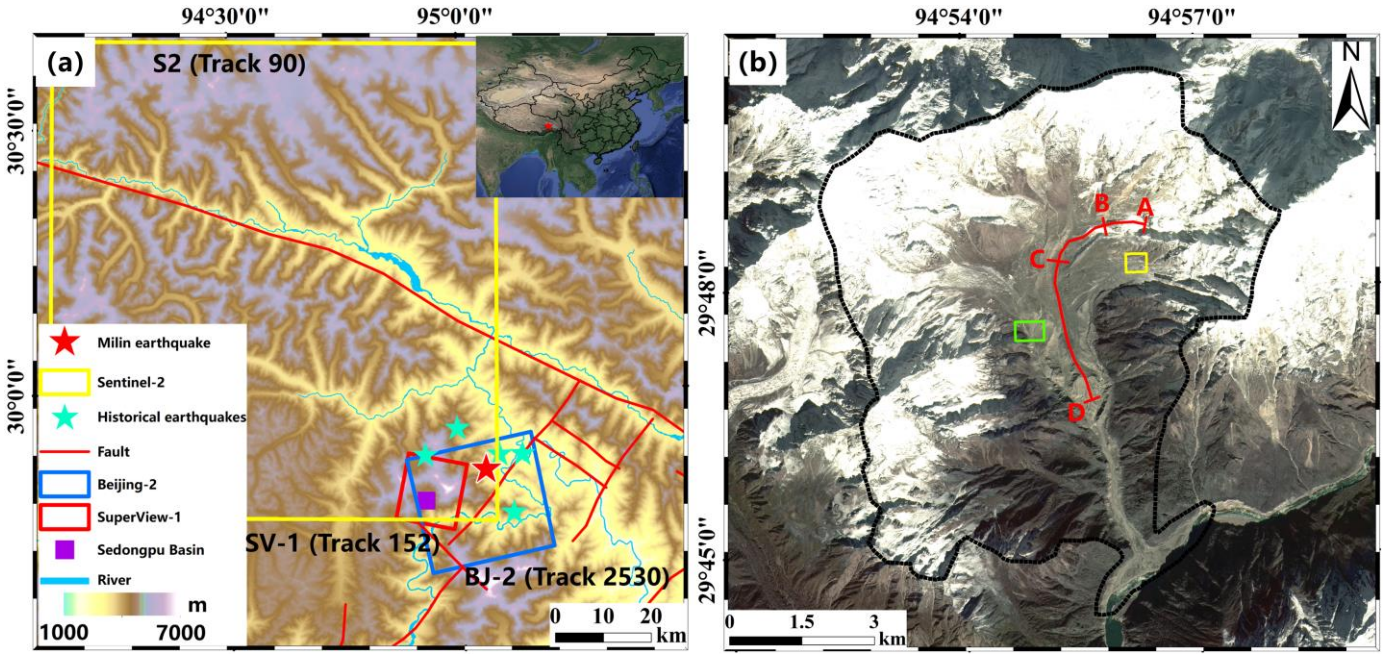


Figure 1. Overview of the study area. (**a**) Image footprints of the Sentinel-2 (S2), Beijing-2 (BJ-2), and SuperView-1 (SV-1) used in this study with a shaded 30 m Shuttle Radar Topography Mission (SRTM) digital elevation model (DEM) as the background. Fault data and seismicity activities with a magnitude above four were downloaded from the Chinese Earthquake Network Center (http://www.ceic.ac.cn/, accessed on 20 December 2023). (**b**) Enlarged topography of the Sedongpu Basin. The black line defines the extent of the Sedongpu basin, the yellow and green rectangles represent two representative stable areas, and the red line represents the profile A-B-C-D along the glacier flow direction.

2.2. Datasets

Due to the remote alpine valley location of the study area and the cloud cover on optical images, multi-temporal optical images were used, including moderate resolution and high-frequency revisit Sentinel-2 images, as well as high-resolution SuperView-1 (SV-1) and Beijing-2 (BJ-2), as shown in Table 1. Since different bands of the same sensor have different spatial resolutions and spectral channels [41,42], we chose near-infrared (NIR) band Sentinel-2 images for their strong atmospheric penetration and noise resistance features [43,44]. In addition, the panchromatic band of the SV-1 image with 0.5 m spatial resolution and BJ-2 image with 0.8 m spatial resolution were acquired on 7 November 2017 and 21 December 2017, respectively.

Table 1. Parameters of optical images used in this study.

Optical Images	Sentinel-2	SV-1	BJ-2
Band	NIR	Panchromatic	Panchromatic
Resolution (m)	10	0.5	0.8
Numbers	6	1	1
Acquisition dates	November 2016–December 2017	7 November 2017	21 December 2017

The scheme with the cross-platform optical images related to Milin earthquake on 18 November 2017 is given in Table 2. Since most Sentinel-2 images before Milin earthquake were covered by heavy clouds, only four images with cloud cover below 5% were chosen for the inversion of pre-seismic displacement. During the earthquake, an image pair combining SV-1 and BJ-2 images were utilized to invert the co-seismic glacier displacement. Lastly, as a river blockage disaster occurred on 21 December 2017, the images before and after the disaster are not correlated, only two Sentinel-2 images were selected for the post-seismic displacement inversion.

Table 2. Multi-temporal optical images in Sedongpu area for pre-, co-, and post-seismic glacier displacement monitoring.

Events	Optical Images	Dates	Stages
Milin earthquake	Sentinel-2	20 November 2016	pre-seismic
	Sentinel-2	10 December 2016	
	Sentinel-2	19 January 2017	
	Sentinel-2	18 February 2017	
	SV-1	7 November 2017	co-seismic
		18 November 2017	
	BJ-2	21 December 2017	
	Sentinel-2	10 December 2017	post-seismic
	Sentinel-2	20 December 2017	
Disaster chain		21 December 2017	

3. Methodology

To research the acceleration and triggering effect of the Ms 6.9 Milin earthquake on the Sedongpu glacier and disaster chain, we propose a two-dimensional displacement time series monitoring strategy with multi-temporal optical images. The Sentinel-2 images are used to invert the displacement before and after the Milin earthquake, and SV-1 and BJ-2 images are employed to invert the co-seismic displacement, including image pair selection, image registration, image correlation calculation, error correction, displacement rate inversion, and accuracy evaluation, which is shown in Figure 2. In order to invert the large gradient glacier displacement, we propose two improved strategies, that is, a four-quadrant block image registration to correct systematic errors and the fusion of the image correlation results calculated within different window sizes to correct gross errors.

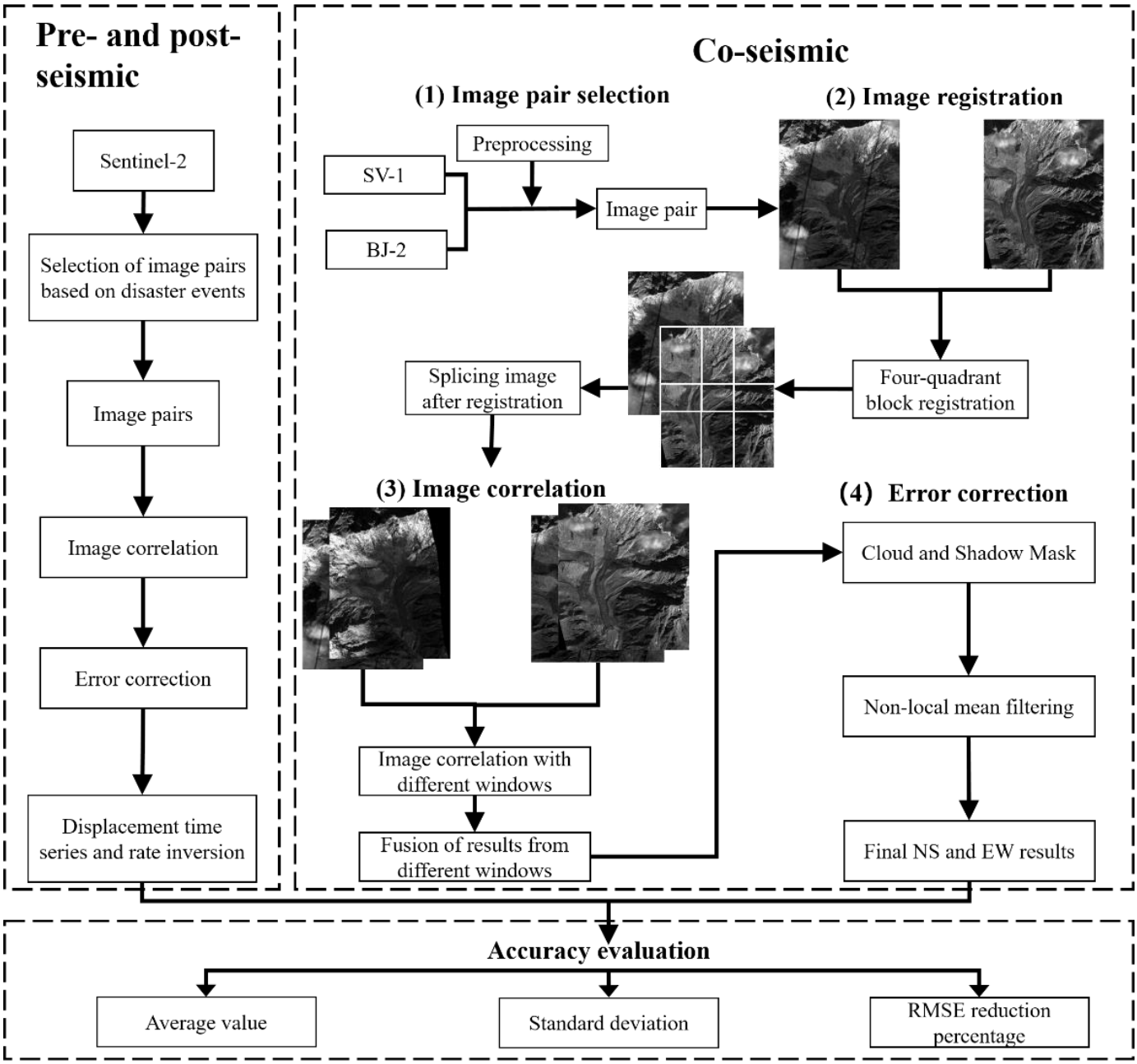


Figure 2. Flowchart of pre-, co-, and post-seismic glacier displacement monitoring and accuracy evaluation with multi-temporal optical image correlation.

3.1. Pre-Processing

3.1.1. Image Pairs Generation

Accounting for the overlapping areas and cloud coverage of the optical images, firstly, six image pairs are generated from four pre-seismic Sentinel-2 images to estimate the pre-seismic glacier displacement; secondly, one co-seismic image pair is generated with cross-platform SV-1 and BJ-2 images; lastly, one image pair is generated with two post-seismic Sentinel-2 images, which are shown in Table 3. To analyze co-seismic and post-seismic displacements, the post-seismic displacement was subtracted during the co-seismic displacement monitoring process.

Table 3. Image pairs generated for three-stage glacier displacement monitoring.

Period	Image Pairs
Pre-seismic	20 November 2016–10 December 2016 20 November 2016–19 January 2017 20 November 2016–18 February 2017 10 December 2016–19 January 2017 10 December 2016–18 February 2017 19 January 2017–18 February 2017
Co-seismic	7 November 2017 (SV-1)–21 December 2017 (BJ-2) excludes 10 December 2017–20 December 2017
Post-seismic	10 December 2017–20 December 2017

3.1.2. Four-Quadrant Block Image Registration

As Sentinel-2 images undergo pre-download calibration, it can ensure a high geocoding accuracy to derive surface horizontal displacement with an optical image correlation technique [45]. However, as the geo-location uncertainties of SV-1 and BJ-2 images are about tens of meters, it is necessary to register them with a certain accuracy before image correlation to estimate the displacement. This study employs a fast and robust matching framework for multimodal image registration. A detailed description of the matching framework can be found in the research [46]. However, the main limitation of cross-platform image co-registration is that it can hardly process the images with large rotation and scale differences. Specifically, the BJ-2 image of 21 December 2017 has a larger geographic location bias, leading to larger registration errors. To address this problem, we propose a four-quadrant block registration strategy, which divides the entire image into four blocks corresponding to the four quadrants. The window size is optimized to obtain reliable displacement results and a common overlap between neighboring windows to maintain spatial consistency across the results. Therefore, the improved registration strategy shown in Figure 3 includes three steps: (a) Segmenting the images into blocks according to four quadrants; (b) Registering each block with the master image using a fast and robust matching framework; (c) Splicing each of the registered blocks into the entire registered image.

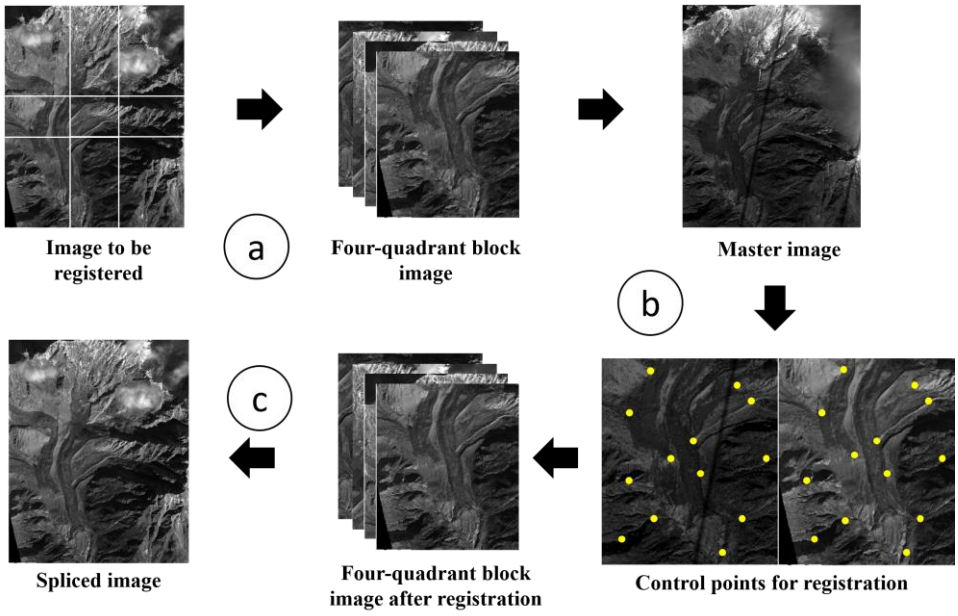


Figure 3. Technical flowchart of the four-quadrant block image registration method.

3.2. Multi-Window Fusion Method

The image correlation was conducted with the Co-registration of Optically Sensed Images and Correlation (COSI-Corr 2014) software package [47] to invert the ground displacement in sub-pixel accuracy between optical images. It is essential to configure parameters to acquire horizontal displacement between each image pair. To unify the spatial resolution of SV-1 and BJ-2 images, they are downsampled to 2 m. The initial and final search window sizes for SV-1 and BJ-2 images are set as 256 and 32, with a search step as 4 × 4 pixels. Whereas they are set as 64 and 32, with a search step of 1 × 1 pixel for Sentinel-2 images. Besides, the correlation threshold and iteration are set as 0.9 and 2, respectively [48]. Specific correlation parameters are detailed in Table 4. Subsequently, the COSI-Corr frequency correlator is utilized to derive the east–west (E/W), north–south (N/S) displacement, and signal-to-noise ratio (SNR). Finally post-processing are carried out to eliminate gross error due to uncorrelation and cloud cover from the original correlation results [49].

Table 4. Parameter configuration for optical images correlation.

Optical Sensors		SV-1, BJ-2	Sentinel-2
Search window size (pixels)	Initial size	256	64
	Final size	32	32
Steps (pixels)		4 × 4	1 × 1
Robust iterations		2	2
Frequency mask		0.9	0.9

In the COSI-Corr software package, the selection of both the initial and final windows is intricately linked to the effectiveness of the Fourier algorithm-based frequency correlator in processing high-quality optical images. The initial window plays a critical role to provide a rough estimation of pixel displacements, while the final window is essential for fine displacement detection at the sub-pixel level. Both parameters change in powers of two [50]. In this study, considering that the spatial resolution of the co-seismic high-resolution image is better than 2 m, the initial window effectively achieves fine estimation of pixel displacement during the image correlation process, resulting in minimal influence from the final window on the results [51]. Therefore, this study focuses on the effect of the initial window on the results. It is worth noting that all subsequent windows mentioned refer to the initial window size. The selection of different windows directly influences the final results. A large window can capture large gradient displacements but may ignore the subtle displacements and errors; conversely, a small window can detect subtle displacements but might underestimate the overall displacement and introduce errors. To improve displacement accuracy and retrieve large gradient displacement, we propose a strategy to fuse correlation results within different windows for monitoring large gradient glacier displacements, as different windows have different abilities to capture displacement. Specifically, the displacement results are robustly estimated based on the results from different windows. For the pre-seismic Sentinel-2 image pairs, the observation equations are given as Equation (1),

$$Bv = d \tag{1}$$

where d is the displacement vector derived from the image correlation, and B is the coefficient matrix from the corresponding temporal baseline. The glacier displacement velocities can be derived based on the least squares criteria shown in Equation (2).

$$v = \left(B^T P B\right)^{-1} B^T P d \tag{2}$$

where P is the weight matrix. Then the average displacement velocity of the image pair in each successive time interval v can be estimated. However, if B is rank deficiency, then the singular value decomposition (SVD) will be applied. If there are n images, the cumulative

displacement time series D and the normalized displacement velocity $\overline{v}$ at a generic m can be retrieved by Equations (3) and (4), respectively [34].

$$D_m = \begin{cases} 0 \quad (m = 1) \\ \sum_{i=1}^{m-1} v_i t_i (m = 2, \ldots, n) \end{cases} \tag{3}$$

$$\overline{v} = \frac{\sum_{i=1}^{n-1} v_i t_i}{\sum_{i=1}^{n-1} t_i} \tag{4}$$

3.3. Error Correction and Accuracy Evaluation

The gross errors in optical image correlation usually includes uncorrelated errors due to cloud cover or surface material changes, shading errors due to different solar altitude angles, and displacement errors that more than 135° out of the slope direction and do not coincide with the direction of gravity-controlled motion [52,53]. To mitigate these errors and improve the accuracy of the displacements, we take some measures including setting a signal-to-noise ratio (SNR) threshold (>0.90), non-local mean filtering, masking the results 135° out of the slope direction.

Due to the lack of field observations of glacier movement, it was observed that the uncertainty is nearly double on moving targets compared to stable regions [54]. We assess the accuracy by calculating the measurement uncertainty in the stable areas [55,56] in terms of Mean Value (MEV), Standard Deviation (STD), and Root Mean Square Error (RMSE). Among these, MEV can assess overall deviation of the displacement, indicating systematic uncertainty; STD represents the stochastic errors; and RMSE can synthesize the total uncertainty of displacement measurements, defined as follows:

$$\mathrm{RMSE} = \sqrt{\mathrm{MEV}^2 + \mathrm{STD}^2} \tag{5}$$

then the reduction percentage in RMSE can be calculated:

$$\mathrm{RMSE}_{\mathrm{reduc}} = \frac{\mathrm{RMSE}_{\mathrm{after}} - \mathrm{RMSE}_{\mathrm{roi}}}{\mathrm{RMSE}_{\mathrm{roi}}} \times 100\% \tag{6}$$

where $\mathrm{RMSE}_{\mathrm{reduc}}$ denotes the reduction percentage of RMSE, $\mathrm{RMSE}_{\mathrm{after}}$ denotes the RMSE after registration or fusion with different windows, and $\mathrm{RMSE}_{\mathrm{roi}}$ denotes the original RMSE of the result.

4. Results

4.1. Four-Quadrant Block Image Registration

In order to verify the applicability of the cross-platform remote sensing image registration and the improvement of the proposed four-quadrant block registration method, we tested the co-seismic image pair, and the results are shown in Figure 4.

Firstly, as shown in Figure 4e,f,i,j, systematic errors occurred if no registration or only overall registration was applied before image correlation, especially affecting the east–west displacement monitoring. Secondly, as shown in Figure 4g,k, results after top and bottom block registration can correct the systematic errors significantly in both north–south and east–west directions. However, systematic offsets were raised at the overlapped regions between the upper and lower blocks. Lastly, as shown in Figure 4h,l, the four-quadrant block image registration strategy can correct the systematic errors and systematic offsets between the four adjacent blocks in both directions.

To evaluate the effects of the proposed method, two stable regions are selected as illustrated in Figure 1, where the yellow one corresponds to one larger registration error, while the green one corresponds to one smaller registration error. Figure 5a–d show the MEV, STD, and RMSE reduction percentages for four different strategies in these two regions. We can observe from Figure 5 that the MEV values in both directions of

the stable region converge to 0 m, and the STD values significantly decrease, while the percentage of RMSE reduction significantly increases. Specifically, in the green region, the RMSE reductions in the NS direction are 56%, 58%, and 78%, respectively, while in the EW direction, they are 82%, 90%, and 89%, respectively. In the yellow region, the large registration error causes the RMSE value to increase instead of decrease after overall registration. So a decrease in RMSE of -54%, 20%, and 89% was observed in the NS direction, and a decrease of -129%, 4%, and 85% was observed in the EW direction.

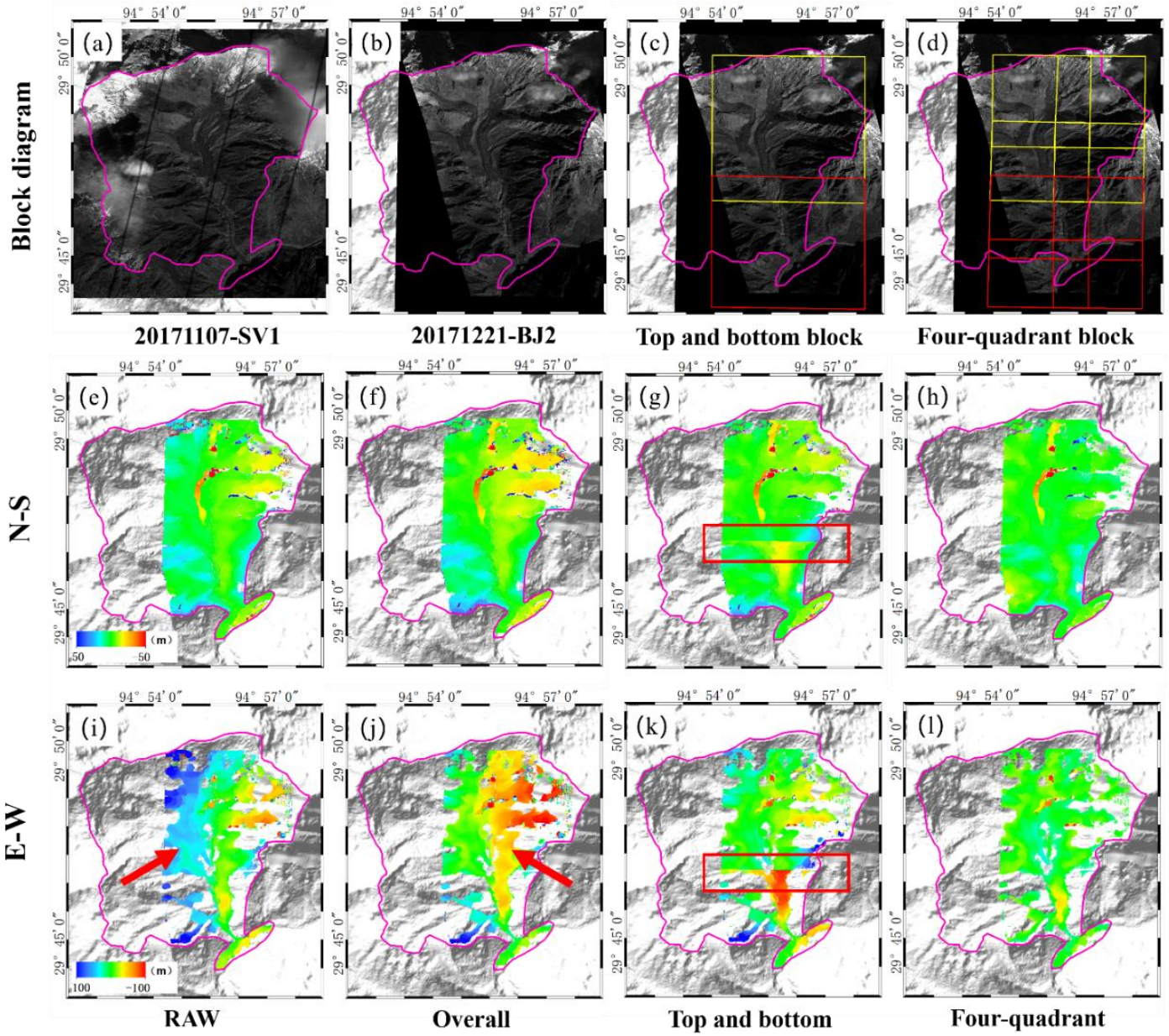


Figure 4. Optical image correlation results for image pair acquired on 7 November 2017 and 21 December 2017 with different registration strategies. The first row (**a**–**d**) is block diagrams, the second row (**e**–**h**) is the north–south results, and the third row (**i**–**l**) is the east–west results. (**e**,**i**) are the results without registration, (**f**,**j**) are the results after overall registration, (**g**,**k**) are the results after top and bottom block registration, and (**h**,**l**) are the results after four-quadrant block registration.

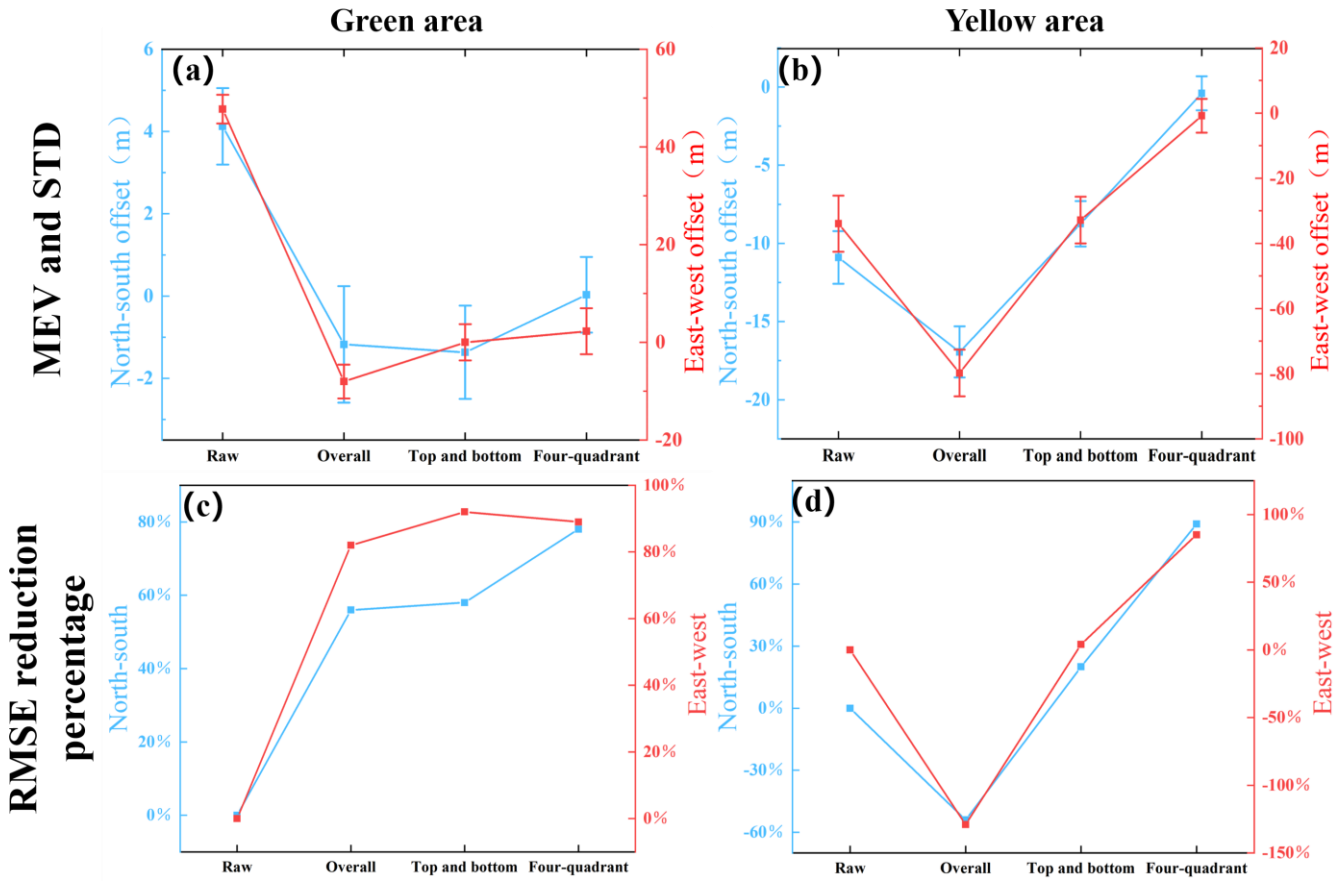


Figure 5. The accuracy evaluation of four registration methods was conducted over two stable areas indicated in Figure 1. (**a**,**b**) are the Mean Value (MEV) and Standard Deviation (STD) of the N–S and E–W displacement in the green and yellow regions, respectively. (**c**,**d**) are the reduction percentage of Root Mean Square Error (RMSE) in the green and yellow areas, respectively.

4.2. Multi-Window Fusion Method

The window size is a key parameter influencing the quality of the optical image correlation results. The experiments with different windows are shown in Figure 6, where notable discrepancies can be seen among various windows. In general, the small window size presents more comprehensive displacement but with a higher proportion of errors. Conversely, the large windows can get coarser displacement with less errors. which is consistent with the previous findings [51].

Figure 6 shows the displacement in the north–south and east–west directions using correlation window sizes of 64, 128, 256, and 512 pixels, where the window size of 64 pixels is relatively inadequate to capture the displacement zone, whereas the one with 128 pixels can detect the displacement in the lower part of the glacier, but is less effective in the upper part with large gradient displacements. Meanwhile, the one with 256 pixels can detect the large gradient displacements in the upper part of the glacier well, but it may ignore the displacement magnitude in the lower part. Lastly, the result with 512 pixels can hardly obtain useful information. Therefore, we robustly fuse the displacement from the four windows to achieve a more comprehensive and accurate displacement field. The final displacement in the north–south and east–west directions are presented in Figure 6i,j.

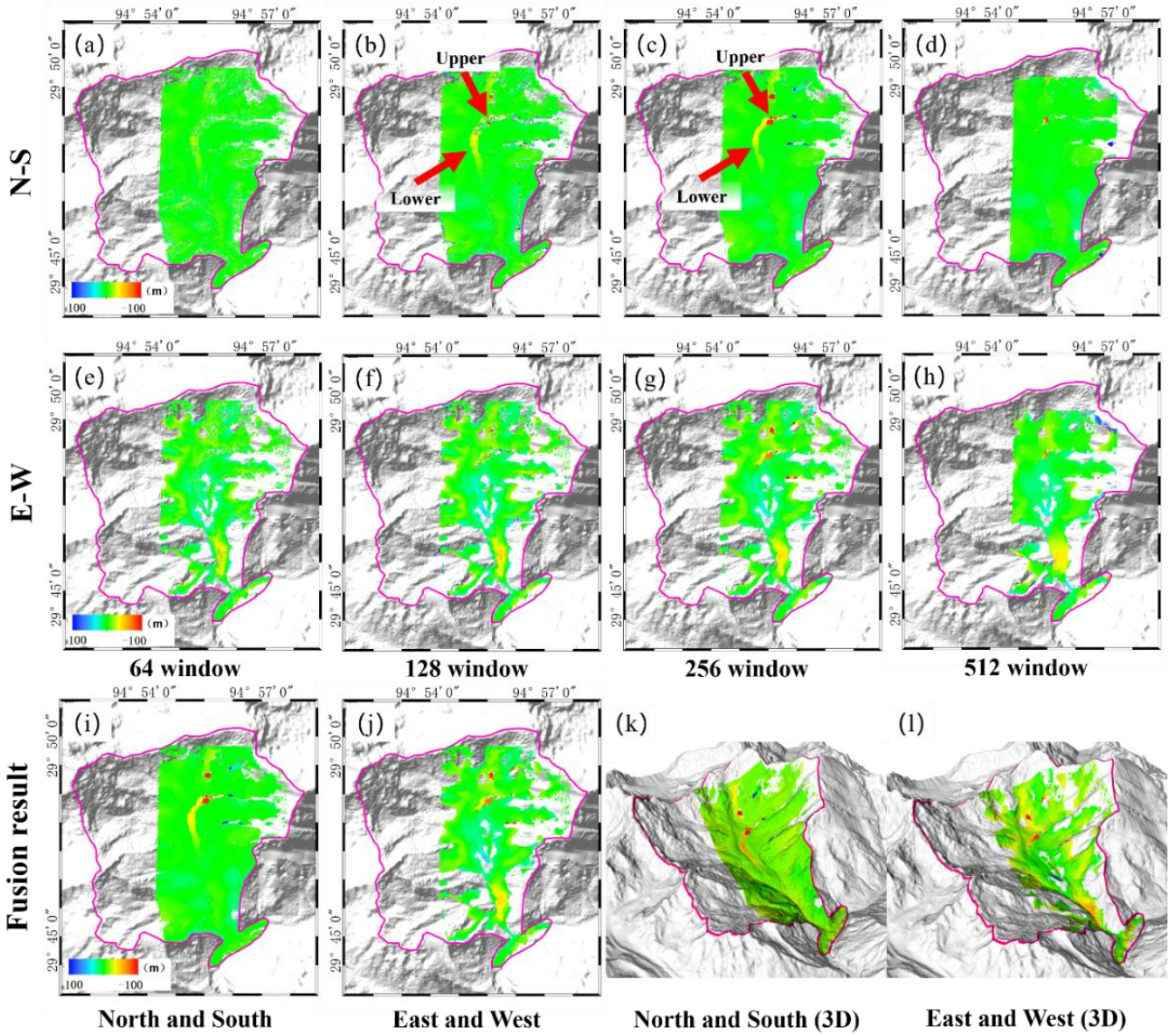


Figure 6. Optical image correlation results with different window sizes. (**a**–**d**) are north–south results, (**e**–**h**) are east–west results, (**i**–**l**) are fusion results from different window sizes shown in 2D and 3D DEM.

We take MEV, STD, and RMSE reduction percentages (refer to the results with 64 windows) to assess the displacement accuracy with four different windows and multi-window fusion in the yellow and green stable zones, as depicted in Figure 7. Firstly, the MEVs are close to 0 m for five cases, except for the east–west direction in the yellow area. Secondly, it is evident that the larger the window size, the smaller the STD, which is consistent with the previous findings [51]. On the contrary, the smaller window size is more sensitive to surface displacement but has a larger STD. However, with significant displacement magnitudes, small windows may become uncorrelated to increase errors. On the contrary, large windows are beneficial for detecting large displacements with high accuracy, but they will blur the displacement boundary, resulting in incomplete displacement results. Lastly, the RMSE reduction percentages for the results using 128, 256, and 512 windows and multi-window fusion referring to the 64 window in the green region are 37%, 55%, 58%, and 56% in the NS direction, and 14%, 23%, 28% and 24% in the EW direction, respectively. In the yellow region, the percentages are 0%, 15%, 26%, and 16% in the NS direction, and 5%, 20%, 41%, and 21% in the EW direction, respectively. Although the 512 window achieves the highest enhancement rate, it also removes displacement information along

with noise. In contrast, the fusion method not only maintains accuracy but also effectively captures a significant amount of displacement information. In summary, the fusion from four windows can balance the displacement magnitude and accuracy.

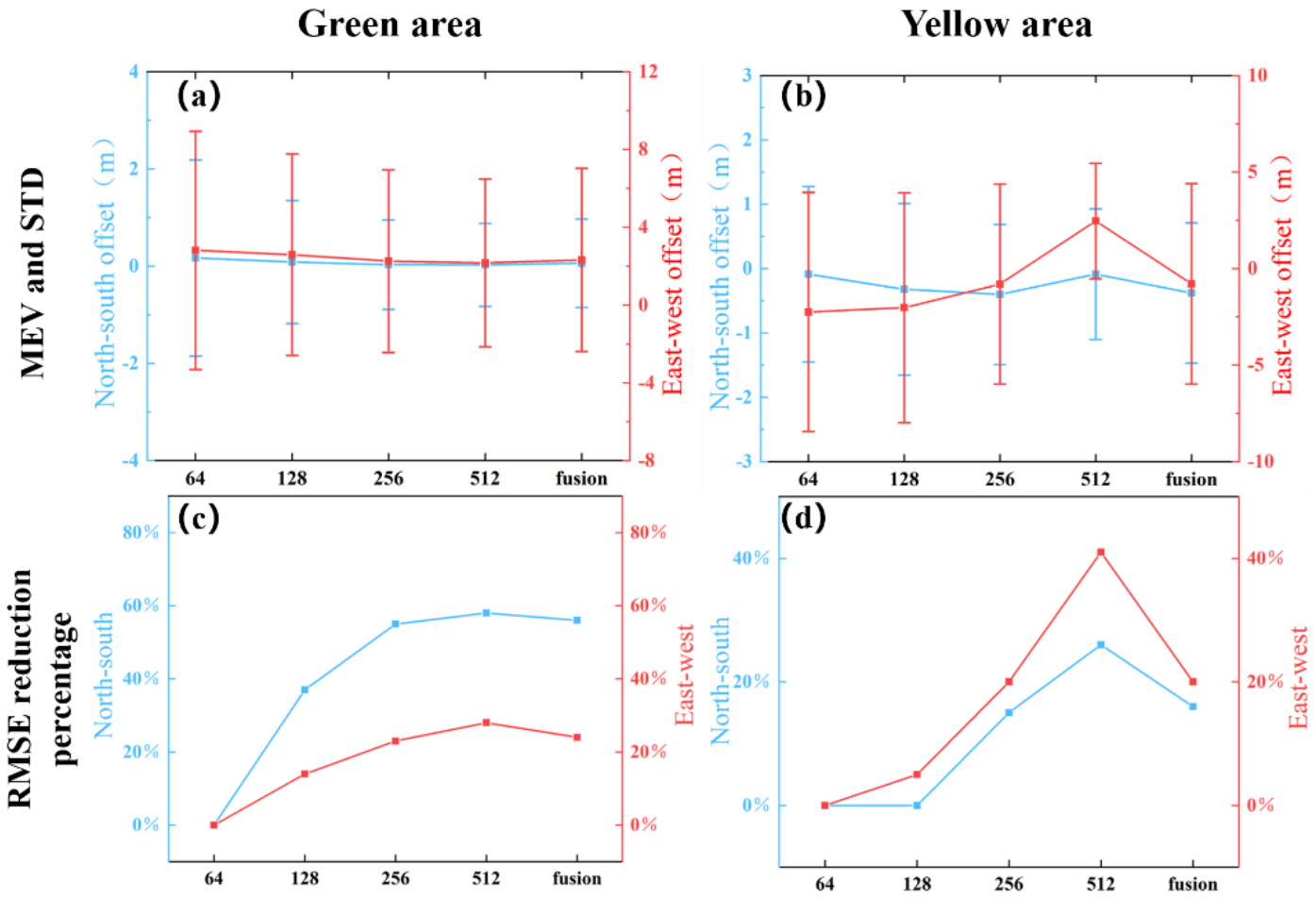


Figure 7. Accuracy evaluation for different window sizes was conducted over two stable areas indicated in Figure 1. (**a**,**b**) the MEV and STD of the N–S and E–W displacement; (**c**,**d**) the RMSE reduction percentage in the green and yellow areas, respectively.

4.3. Two-Dimensional Displacement Field of Sedongpu Glacier

To better understand the dynamics of the Sedongpu Glacier, we integrate the east–west and north–south displacement results from optical image correlation into a two-dimensional displacement field, which reflects the horizontal displacement of the Sedongpu glacier. Figure 8 shows that the primary displacement time series of the Sedongpu Glacier predominantly occurred within one main gully and five branch gullies during three phases: pre-seismic, co-seismic, and post-seismic.

The cumulative displacement of the glacier in three stages can be obtained from Figure 8, that is, the pre-seismic glacier displacement ranged from 20–40 m from 20 November 2016 to 18 February 2017; the maximum co-seismic displacement from 7 November to 10 December 2017 was 210.3 m in the acceleration section, 104.6 m in the flow direction change section, and 29.2 m in the transportation section; and the post-seismic displacement ranged from 10 to 20 m from 10 December to 20 December 2017.

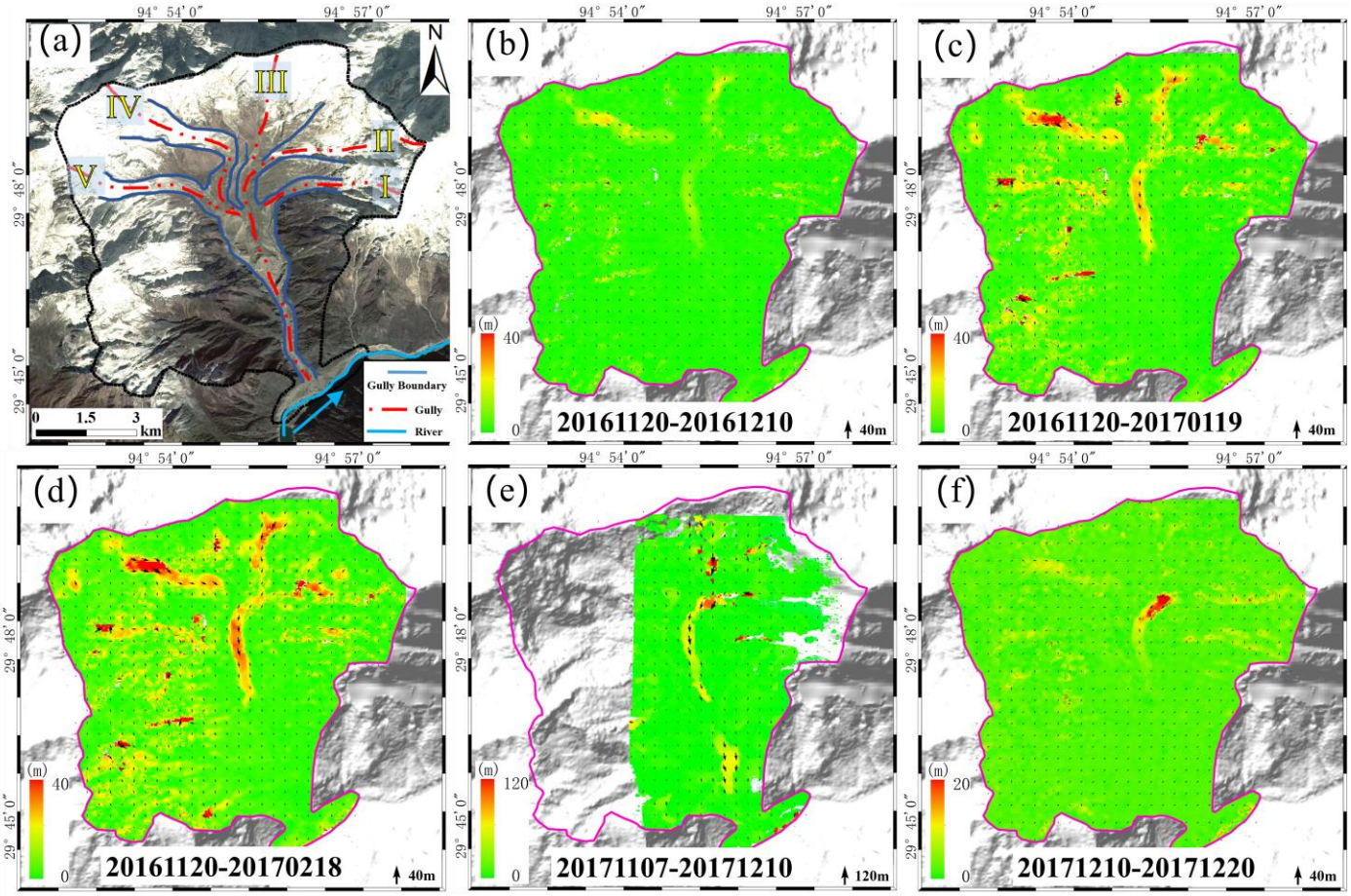


Figure 8. Displacement magnitudes and directions for three stages during the pre-, co-, and post-seismic periods. (**a**) Show the gully distribution with I–V and the direction of the glacial displacement. (**b**–**d**) are the pre-seismic displacement field from Sentinel-2 images, (**e**) the co-seismic high-resolution displacement field, (**f**) the post-seismic displacement field from Sentinel-2 images.

5. Discussion

5.1. Acceleration on Sedongpu Glacier Movement by Milin Earthquake

To reveal the correlation between the Milin earthquake and the Sedongpu glacier movement, we calculate the daily displacement rates during three stages: pre-seismic, co-seismic, and post-seismic. The displacement rates along profiles A–D during the three stages are presented in Figure 9d. The direction of glacier displacement is indicated by black arrows in Figure 9.

It reveals different spatiotemporal features along the main Sedongpu glacier from Figure 9d. Firstly, three displacement sections can be segmented, including the acceleration section, flow direction change section, and transportation section corresponding to profile AB, BC, and CD, respectively. The divisions are made based on glacier movement velocity and topography, i.e., section AB has a steeper slope and a significantly faster velocity, section BC is the area where the movement direction changes, and section CD has a gentler slope and a small change in velocity. The points with obvious changes in topography and velocity are selected for three sections of the division. Secondly, the pre-seismic displacement rates across the three sections were similar, but the co-seismic and post-seismic kinematic characteristics of the three sections changed differently. During the co-seismic period, Section AB had the highest displacement rate, while Section CD had the lowest one. Conversely, during the post-seismic period, Section BC exhibited the highest displacement rate, whereas Sections AB and CD became smaller than in the co-seismic period. Quantitatively, the maximum daily displacement rate in the acceleration section

(profile AB) increased from 0.36 m/day before the Milin earthquake to 6.37 m/day during the earthquake period, then decreased to 1.06 m/day after the earthquake. In addition, moderate acceleration occurred in the flow direction change section (profile BC), increasing from 0.13 m/day before the earthquake to 3.17 m/day during the earthquake, then decreasing to 1.85 m/day after the earthquake. Meanwhile, slight acceleration also occurred in the transportation section (profile CD), increasing from 0.20 m/day to 0.62 m/day, then decreasing to 0.30 m/day. The kinematic connection among the three sections is because Section AB has a steeper slope and is closer to the source ice-avalanche area, Section BC has a gentler slope but in the flow direction change area, and Section CD still has a gentler slope but in the transportation area. In summary, it is certain that the Milin earthquake, which occurred on 18 November 2017, 11 km from the Sedongpu area, significantly accelerated the Sedongpu glacier, especially in the acceleration and flow direction change sections, with the effects lasting until 20 December 2017.

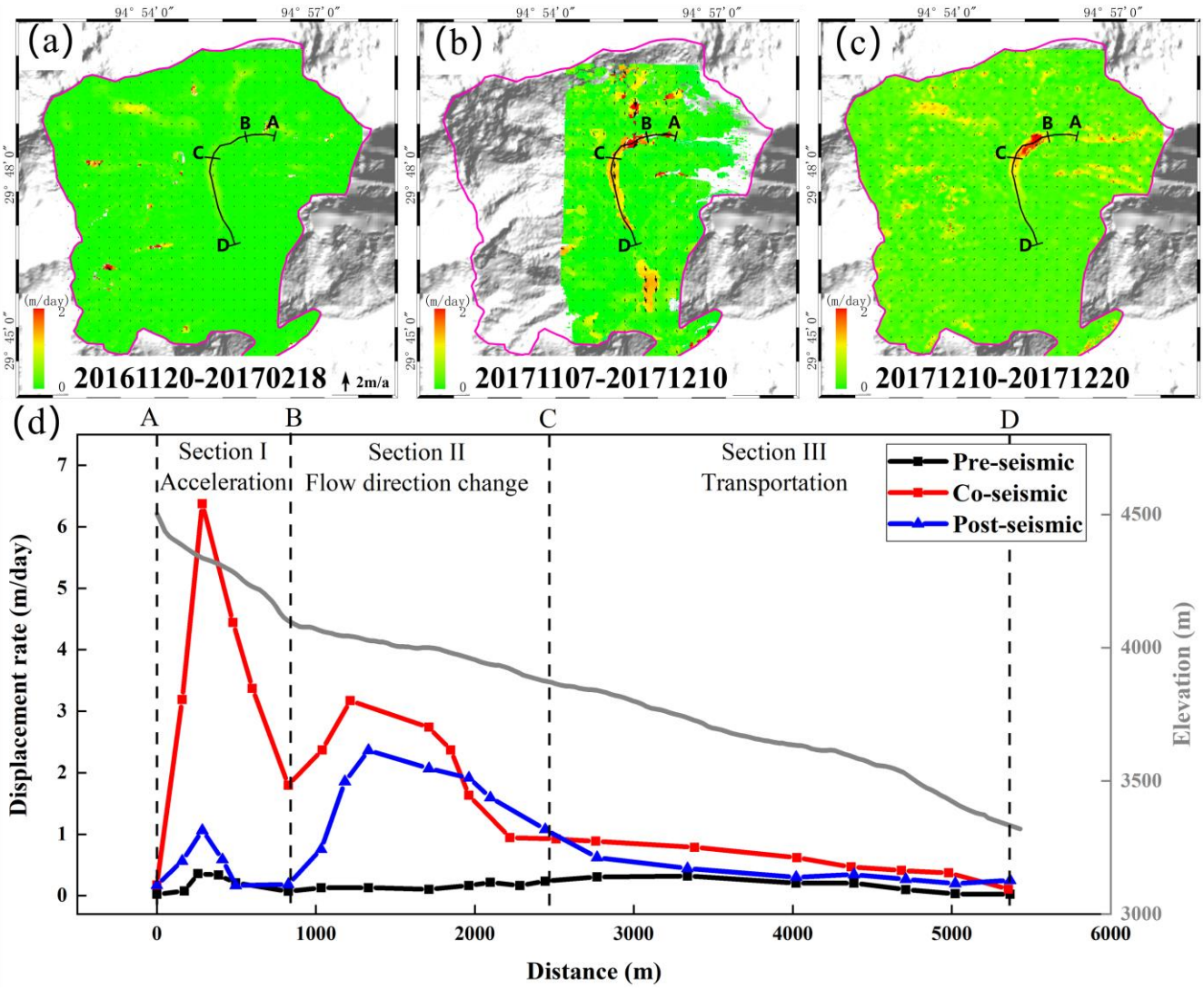


Figure 9. Displacement rate maps and the profile of Sedongpu Glacier at three stages. (**a**–**c**) the daily displacement during the pre-, co-, and post-seismic periods, respectively. (**d**) The profile of daily displacement rate during three stages. The three sections are separated by dashed lines, with section I corresponding to AB, section II to BC, and section III to CD.

5.2. Failure Pattern of the 21 December 2017 Disaster Chain

Strong tectonic activity, frequent earthquakes, increasing global climate change, and strong internal and external dynamics [57] can result in low strength and poor stability of

mountain glaciers. Following the earthquake, a disaster chain occurred in the Sedongpu basin on 21 December 2017, leading to the blockage of the Yarlung Tsangpo River. Notably, there was no heavy rainfall or drastic temperature changes prior to this disaster chain, but glacier movement accelerated significantly. Therefore, it can be inferred that the Milin earthquake had a triggering effect lasting around 33 days on the disaster chain.

Figure 10a,b show the surface changes before and after the disaster chain based on Planet satellite images acquired on 21 December 2017 and 26 December 2017. Figure 10c,d show the failure pattern of the disaster chain in the Sedongpu basin, which can be divided into three different sections: the source area, the moraine area, and deposition area [58]. Firstly, about 0.33 km^2 of ice and rock in the source area collapsed; secondly, according to the monitoring of the moraine area in this paper, the Milin earthquake triggered glacier movement, leading to a cumulative displacement of up to 226 m during the co-seismic and post-seismic periods within 33 days; lastly, 1 million m^3 of sediment transported from the moraine area was finally deposited at the intersection, which pushed the sediment to the river by 200–450 m to form a barrier dam about 0.53 km^2 with an elevation of 2746 m in the Yarlung Tsangpo River. It completely blocked the main channel, raising the water levels by approximately 2 m [59].

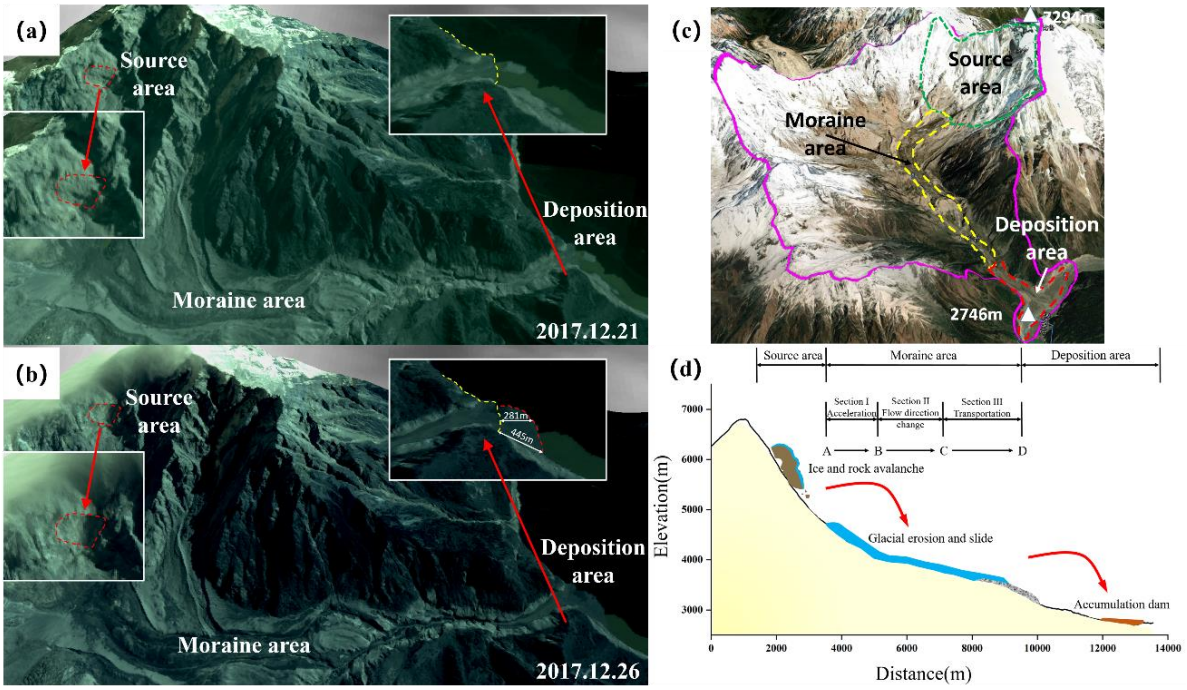


Figure 10. (**a**,**b**) are Planet satellite images from 21 December and 26 December 2017, respectively, used to observe changes before and after the disaster chain. (**c**) The schematic diagram of longitudinal section in Sedongpu. (**d**) The failure pattern of the Sedongpu disaster chain.

The disaster chain that occurred on 21 December 2017 lasted for 33 days and was mainly induced by the Milin earthquake. Later disaster chain events that occurred in the Sedongpu basin indicate that the lagging effects of the Milin earthquake may have lasted for an even longer time.

6. Conclusions

In this study, we propose a two-dimensional displacement time series monitoring strategy with multi-temporal optical images to research the acceleration and triggering effects of the Ms 6.9 Milin earthquake on the Sedongpu glacier and disaster chain, where a four-quadrant block registration strategy and a multi-window fusion strategy were proposed to increase displacement monitoring accuracy for cross-platform optical images.

The RMSE of the new method can decrease 80% of the traditional method. Based on three stages of glacier displacement, the Milin earthquake had a drastic impact on the glacier displacement, accelerating it up to 1–6 m/day. The earthquake had a triggering effect around 33 days on the disaster chain of 21 December 2017. The failure pattern can be summarized as ice and rock collapse in the source area, large magnitude glacier displacement in the moraine area, and a large volume of sediment in the deposition area, causing a river blockage. This study can explain the activation effect and precursory displacement patterns of ice-rock avalanche disaster chain events well, which is beneficial to the monitoring and early warning of disaster chain events in remote mountainous areas.

However, the proposed strategy makes it difficult to deal with multimode images with distinct imaging viewpoints and heavy cloud coverage. Therefore, to improve the reliability, we will collect more multimode data, including LiDAR, SAR, and optical images, for large gradient displacement monitoring.

Author Contributions: Conceptualization, Y.X., C.Z. and J.L.; Data curation, Y.X.; Formal analysis, Y.G.; Funding acquisition, C.Z. and B.L.; Investigation, Y.X., C.Z., B.L. and Y.G.; Methodology, Y.X., X.L. and J.L.; Project administration, B.L.; Resources, C.Z.; Software, Y.X. and B.L.; Supervision, Y.X. and C.Z.; Validation, Y.X., C.Z. and X.L.; Visualization, Y.X.; Writing—original draft, Y.X.; Writing—review & editing, C.Z. All authors have read and agreed to the published version of the manuscript.

Funding: This work was funded by the National Key R&D Program of China (No. 2022YFC3004302).

Data Availability Statement: Data are available from the corresponding author upon reasonable request.

Acknowledgments: Sentinel-2 images were provided by the European Space Agency (https://www.esa.int/, accessed on 10 October 2023). This study was supported by Chang'an University High Performance Computing Platform.

Conflicts of Interest: The authors declare no conflict of interest.

References

1. Allen, S.K.; Cox, S.C.; Owens, I.F. Rock Avalanches and Other Landslides in the Central Southern Alps of New Zealand: A Regional Study Considering Possible Climate Change Impacts. *Landslides* **2011**, *8*, 33–48. [CrossRef]
2. Haeberli, W.; Huggel, C.; Kääb, A.; Zgraggen-Oswald, S.; Polkvoj, A.; Galushkin, I.; Zotikov, I.; Osokin, N. The Kolka-Karmadon Rock/Ice Slide of 20 September 2002: An Extraordinary Event of Historical Dimensions in North Ossetia, Russian Caucasus. *J. Glaciol.* **2004**, *50*, 533–546. [CrossRef]
3. Jacquemart, M.; Loso, M.; Leopold, M.; Welty, E.; Berthier, E.; Hansen, J.S.S.; Sykes, J.; Tiampo, K. What Drives Large-Scale Glacier Detachments? Insights from Flat Creek Glacier, St. Elias Mountains, Alaska. *Geology* **2020**, *48*, 703–707. [CrossRef]
4. Shugar, D.H.; Jacquemart, M.; Shean, D.; Bhushan, S.; Upadhyay, K.; Sattar, A.; Schwanghart, W.; McBride, S.; De Vries, M.V.W.; Mergili, M.; et al. A Massive Rock and Ice Avalanche Caused the 2021 Disaster at Chamoli, Indian Himalaya. *Science* **2021**, *373*, 300–306. [CrossRef] [PubMed]
5. Kääb, A.; Leinss, S.; Gilbert, A.; Bühler, Y.; Gascoin, S.; Evans, S.G.; Bartelt, P.; Berthier, E.; Brun, F.; Chao, W.-A.; et al. Massive Collapse of Two Glaciers in Western Tibet in 2016 after Surge-like Instability. *Nat. Geosci.* **2018**, *11*, 114–120. [CrossRef]
6. Martha, T.R.; Roy, P.; Jain, N.; Vinod Kumar, K.; Reddy, P.S.; Nalini, J.; Sharma, S.V.S.P.; Shukla, A.K.; Durga Rao, K.H.V.; Narender, B.; et al. Rock Avalanche Induced Flash Flood on 07 February 2021 in Uttarakhand, India—A Photogeological Reconstruction of the Event. *Landslides* **2021**, *18*, 2881–2893. [CrossRef]
7. Ahanger, M.A.; Jeelani, G. Deformation Kinematics of Main Central Thrust Zone (MCTZ) in the Western Himalayas. *J. Earth Sci.* **2022**, *33*, 452–461. [CrossRef]
8. Yin, Y.; Xing, A. Aerodynamic Modeling of the Yigong Gigantic Rock Slide-Debris Avalanche, Tibet, China. *Bull. Eng. Geol. Environ.* **2012**, *71*, 149–160. [CrossRef]
9. Chen, G.; Bartholomew, M.; Liu, D.; Cao, K.; Feng, M.; Wang, D. Paleo-Earthquakes along the Zheduotang Fault, Xianshuihe Fault System, Eastern Tibet: Implications for Seismic Hazard Evaluation. *J. Earth Sci.* **2022**, *33*, 1233–1245. [CrossRef]
10. Casagli, N.; Intrieri, E.; Tofani, V.; Gigli, G.; Raspini, F. Landslide Detection, Monitoring and Prediction with Remote-Sensing Techniques. *Nat. Rev. Earth Environ.* **2023**, *4*, 51–64. [CrossRef]
11. Wenjing, Z. Identification of Glaciers with Surge Characteristics on the Tibetan Plateau. *Ann. Glaciol.* **1992**, *16*, 168–172. [CrossRef]
12. Yang, W.; Wang, Z.; An, B.; Chen, Y.; Zhao, C.; Li, C.; Wang, Y.; Wang, W.; Li, J.; Wu, G.; et al. Early Warning System for Ice Collapses and River Blockages in the Sedongpu Valley, Southeastern Tibetan Plateau. *Nat. Hazards Earth Syst. Sci.* **2023**, *23*, 3015–3029. [CrossRef]
13. Delaney, K.B.; Evans, S.G. The 2000 Yigong Landslide (Tibetan Plateau), Rockslide-Dammed Lake and Outburst Flood: Review, Remote Sensing Analysis, and Process Modelling. *Geomorphology* **2015**, *246*, 377–393. [CrossRef]

14. Zhou, J.; Cui, P.; Hao, M. Comprehensive Analyses of the Initiation and Entrainment Processes of the 2000 Yigong Catastrophic Landslide in Tibet, China. *Landslides* **2016**, *13*, 39–54. [CrossRef]
15. Pandey, P.; Chauhan, P.; Bhatt, C.M.; Thakur, P.K.; Kannaujia, S.; Dhote, P.R.; Roy, A.; Kumar, S.; Chopra, S.; Bhardwaj, A.; et al. Cause and Process Mechanism of Rockslide Triggered Flood Event in Rishiganga and Dhauliganga River Valleys, Chamoli, Uttarakhand, India Using Satellite Remote Sensing and in Situ Observations. *J. Indian. Soc. Remote Sens.* **2021**, *49*, 1011–1024. [CrossRef]
16. Cook, K.L.; Rekapalli, R.; Dietze, M.; Pilz, M.; Cesca, S.; Rao, N.P.; Srinagesh, D.; Paul, H.; Metz, M.; Mandal, P.; et al. Detection and Potential Early Warning of Catastrophic Flow Events with Regional Seismic Networks. *Science* **2021**, *374*, 87–92. [CrossRef]
17. Gao, H.; Gao, Y.; Li, B.; Yin, Y.; Yang, C.; Wan, J.; Zhang, T. The Dynamic Simulation and Potential Hazards Analysis of the Yigong Landslide in Tibet, China. *Remote Sens.* **2023**, *15*, 1322. [CrossRef]
18. Kääb, A.; Treichler, D.; Nuth, C.; Berthier, E. Brief Communication: Contending Estimates of 2003–2008 Glacier Mass Balance over the Pamir–Karakoram–Himalaya. *Cryosphere* **2015**, *9*, 557–564. [CrossRef]
19. Yin, Y.; Li, B.; Gao, Y.; Wang, W.; Zhang, S.; Zhang, N. Geostructures, Dynamics and Risk Mitigation of High-Altitude and Long-Runout Rockslides. *J. Rock. Mech. Geotech. Eng.* **2023**, *15*, 66–101. [CrossRef]
20. Zhang, T.; Yin, Y.; Li, B.; Liu, X.; Wang, M.; Gao, Y.; Wan, J.; Gnyawali, K.R. Characteristics and Dynamic Analysis of the February 2021 Long-Runout Disaster Chain Triggered by Massive Rock and Ice Avalanche at Chamoli, Indian Himalaya. *J. Rock Mech. Geotech. Eng.* **2023**, *15*, 296–308. [CrossRef]
21. Zhang, T.; Gao, Y.; Li, B.; Yin, Y.; Liu, X.; Gao, H.; Yang, W. Characteristics of Rock-Ice Avalanches and Geohazard-Chains in the Parlung Zangbo Basin, Tibet, China. *Geomorphology* **2023**, *422*, 108549. [CrossRef]
22. Gao, Y.; Li, B.; Gao, H.; Gao, S.; Wang, M.; Liu, X. Risk Assessment of the Sedongpu High-Altitude and Ultra-Long-Runout Landslide in the Lower Yarlung Zangbo River, China. *Bull. Eng. Geol. Environ.* **2023**, *82*, 360. [CrossRef]
23. Hu, K.; Zhang, X.; You, Y.; Hu, X.; Liu, W.; Li, Y. Landslides and Dammed Lakes Triggered by the 2017 Ms6.9 Milin Earthquake in the Tsangpo Gorge. *Landslides* **2019**, *16*, 993–1001. [CrossRef]
24. Xiong, W.; Chen, W.; Wen, Y.; Liu, G.; Nie, Z.; Qiao, X.; Xu, C. Insight into the 2017 Mainling Mw 6.5 Earthquake: A Complicated Thrust Event beneath the Namche Barwa Syntaxis. *Earth Planets Space* **2019**, *71*, 71. [CrossRef]
25. Zhang, T.; Yin, Y.; Li, B.; Gao, Y.; Wang, M. Characteristics and Dynamic Analysis of the October 2018 Long-Runout Disaster Chains in the Yarlung Zangbo River Downstream, Tibet, China. *Nat. Hazards* **2022**, *113*, 1563–1582. [CrossRef]
26. Fischer, L.; Huggel, C.; Kääb, A.; Haeberli, W. Slope Failures and Erosion Rates on a Glacierized High-mountain Face under Climatic Changes. *Earth Surf. Process. Landf.* **2013**, *38*, 836–846. [CrossRef]
27. Scaioni, M.; Longoni, L.; Melillo, V.; Papini, M. Remote Sensing for Landslide Investigations: An Overview of Recent Achievements and Perspectives. *Remote Sens.* **2014**, *6*, 9600–9652. [CrossRef]
28. Avouac, J.-P.; Leprince, S. Geodetic Imaging Using Optical Systems. In *Treatise on Geophysics*; Elsevier: Amsterdam, The Netherlands, 2015; pp. 387–424, ISBN 978-0-444-53803-1.
29. Leprince, S.; Barbot, S.; Ayoub, F.; Avouac, J.-P. Automatic and Precise Orthorectification, Coregistration, and Subpixel Correlation of Satellite Images, Application to Ground Deformation Measurements. *IEEE Trans. Geosci. Remote Sens.* **2007**, *45*, 1529–1558. [CrossRef]
30. Altena, B.; Scambos, T.; Fahnestock, M.; Kääb, A. Extracting Recent Short-Term Glacier Velocity Evolution over Southern Alaska and the Yukon from a Large Collection of Landsat Data. *Cryosphere* **2019**, *13*, 795–814. [CrossRef]
31. Bontemps, N.; Lacroix, P.; Doin, M.-P. Inversion of Deformation Fields Time-Series from Optical Images, and Application to the Long Term Kinematics of Slow-Moving Landslides in Peru. *Remote Sens. Environ.* **2018**, *210*, 144–158. [CrossRef]
32. Mazzanti, P.; Caporossi, P.; Muzi, R. Sliding Time Master Digital Image Correlation Analyses of CubeSat Images for Landslide Monitoring: The Rattlesnake Hills Landslide (USA). *Remote Sens.* **2020**, *12*, 592. [CrossRef]
33. Stumpf, A.; Michéa, D.; Malet, J.-P. Improved Co-Registration of Sentinel-2 and Landsat-8 Imagery for Earth Surface Motion Measurements. *Remote Sens.* **2018**, *10*, 160. [CrossRef]
34. Ding, C.; Zhang, L.; Liao, M.; Feng, G.; Dong, J.; Ao, M.; Yu, Y. Quantifying the Spatio-Temporal Patterns of Dune Migration near Minqin Oasis in Northwestern China with Time Series of Landsat-8 and Sentinel-2 Observations. *Remote Sens. Environ.* **2020**, *236*, 111498. [CrossRef]
35. Ding, C.; Feng, G.; Zhang, L.; Shen, Q.; Xiong, Z.; Liao, M. The Precursory 3D Displacement Patterns and Their Implicit Collapse Mechanism of the Ice-Rock Avalanche Events Occurred in Sedongpu Basin Revealed by Optical and SAR Observations. *Remote Sens.* **2023**, *15*, 2818. [CrossRef]
36. Yang, C.; Wei, C.; Ding, H.; Wei, Y.; Zhu, S.; Li, Z. Inversion of Glacier 3D Displacement from Sentinel-1 and Landsat 8 Images Based on Variance Component Estimation: A Case Study in Shishapangma Peak, Tibet, China. *Remote Sens.* **2022**, *15*, 4. [CrossRef]
37. Zhao, C.; Chen, L.; Yin, Y.; Liu, X.; Li, B.; Ren, C.; Liu, D. Failure Process and Three-Dimensional Motions of Mining-Induced Jianshanying Landslide in China Observed by Optical, LiDAR and SAR Datasets. *GIScience Remote Sens.* **2023**, *60*, 2268367. [CrossRef]
38. Li, Y.; Cui, Y.; Hu, X.; Lu, Z.; Guo, J.; Wang, Y.; Wang, H.; Wang, S.; Zhou, X. Glacier Retreat in Eastern Himalaya Drives Catastrophic Glacier Hazard Chain. *Geophys. Res. Lett.* **2024**, *51*, e2024GL108202. [CrossRef]
39. Zhao, B.; Li, W.; Wang, Y.; Lu, J.; Li, X. Landslides Triggered by the Ms 6.9 Nyingchi Earthquake, China (18 November 2017): Analysis of the Spatial Distribution and Occurrence Factors. *Landslides* **2019**, *16*, 765–776. [CrossRef]

40. Zhang, T. Massive Glacier-Related Geohazard Chains and Dynamics Analysis at the Yarlung Zangbo River Downstream of Southeastern Tibetan Plateau. *Bull. Eng. Geol. Environ.* **2023**, *82*, 426. [CrossRef]
41. Necsoiu, M.; Leprince, S.; Hooper, D.M.; Dinwiddie, C.L.; McGinnis, R.N.; Walter, G.R. Monitoring Migration Rates of an Active Subarctic Dune Field Using Optical Imagery. *Remote Sens. Environ.* **2009**, *113*, 2441–2447. [CrossRef]
42. Scherler, D.; Leprince, S.; Strecker, M. Glacier-Surface Velocities in Alpine Terrain from Optical Satellite Imagery—Accuracy Improvement and Quality Assessment. *Remote Sens. Environ.* **2008**, *112*, 3806–3819. [CrossRef]
43. Ayoub, F.; Leprince, S.; Binet, R.; Lewis, K.W.; Aharonson, O.; Avouac, J.-P. Influence of Camera Distortions on Satellite Image Registration and Change Detection Applications. In Proceedings of the IGARSS 2008—2008 IEEE International Geoscience and Remote Sensing Symposium, Boston, MA, USA, 7–11 July 2008; IEEE: Boston, MA, USA, 2008; pp. II-1072–II-1075.
44. Vermeesch, P.; Drake, N. Remotely Sensed Dune Celerity and Sand Flux Measurements of the World's Fastest Barchans (Bodélé, Chad). *Geophys. Res. Lett.* **2008**, *35*, 2008GL035921. [CrossRef]
45. Loveland, T.R.; Irons, J.R. Landsat 8: The Plans, the Reality, and the Legacy. *Remote Sens. Environ.* **2016**, *185*, 1–6. [CrossRef]
46. Ye, Y.; Bruzzone, L.; Shan, J.; Bovolo, F.; Zhu, Q. Fast and Robust Matching for Multimodal Remote Sensing Image Registration. *IEEE Trans. Geosci. Remote Sens.* **2019**, *57*, 9059–9070. [CrossRef]
47. Ayoub, F.; Leprince, S.; Keene, L. *User's Guide to COSI-CORR Co-Registration of Optically Sensed Images and Correlation*; California Institute of Technology: Pasadena, CA, USA, 2009; Volume 38, p. 49s.
48. Baird, T.; Bristow, C.; Vermeesch, P. Measuring Sand Dune Migration Rates with COSI-Corr and Landsat: Opportunities and Challenges. *Remote Sens.* **2019**, *11*, 2423. [CrossRef]
49. Ding, C.; Feng, G.; Li, Z.; Shan, X.; Du, Y.; Wang, H. Spatio-Temporal Error Sources Analysis and Accuracy Improvement in Landsat 8 Image Ground Displacement Measurements. *Remote Sens.* **2016**, *8*, 937. [CrossRef]
50. Leprince, S.; Ayoub, F.; Klinger, Y.; Avouac, J.-P. Co-Registration of Optically Sensed Images and Correlation (COSI-Corr): An Operational Methodology for Ground Deformation Measurements. In Proceedings of the 2007 IEEE International Geoscience and Remote Sensing Symposium, Barcelona, Spain, 23–27 July 2007; IEEE: Barcelona, Spain, 2007; pp. 1943–1946.
51. Yang, W.; Wang, Y.; Wang, Y.; Ma, C.; Ma, Y. Retrospective Deformation of the Baige Landslide Using Optical Remote Sensing Images. *Landslides* **2020**, *17*, 659–668. [CrossRef]
52. Kääb, A. Combination of SRTM3 and Repeat ASTER Data for Deriving Alpine Glacier Flow Velocities in the Bhutan Himalaya. *Remote Sens. Environ.* **2005**, *94*, 463–474. [CrossRef]
53. Stumpf, A.; Malet, J.-P.; Allemand, P.; Ulrich, P. Surface Reconstruction and Landslide Displacement Measurements with Pléiades Satellite Images. *ISPRS J. Photogramm. Remote Sens.* **2014**, *95*, 1–12. [CrossRef]
54. Dehecq, A.; Gourmelen, N.; Trouve, E. Deriving Large-Scale Glacier Velocities from a Complete Satellite Archive: Application to the Pamir–Karakoram–Himalaya. *Remote Sens. Environ.* **2015**, *162*, 55–66. [CrossRef]
55. Ali, E.; Xu, W.; Ding, X. Improved Optical Image Matching Time Series Inversion Approach for Monitoring Dune Migration in North Sinai Sand Sea: Algorithm Procedure, Application, and Validation. *ISPRS J. Photogramm. Remote Sens.* **2020**, *164*, 106–124. [CrossRef]
56. Lacroix, P.; Bièvre, G.; Pathier, E.; Kniess, U.; Jongmans, D. Use of Sentinel-2 Images for the Detection of Precursory Motions before Landslide Failures. *Remote Sens. Environ.* **2018**, *215*, 507–516. [CrossRef]
57. Ding, L.; Zhong, D.; Yin, A.; Kapp, P.; Harrison, T.M. Cenozoic Structural and Metamorphic Evolution of the Eastern Himalayan Syntaxis (Namche Barwa). *Earth Planet. Sci. Lett.* **2001**, *192*, 423–438. [CrossRef]
58. Gao, H.; Yin, Y.; Li, B.; Gao, Y.; Zhang, T.; Liu, X.; Wan, J. Geomorphic Evolution of the Sedongpu Basin after Catastrophic Ice and Rock Avalanches Triggered by the 2017 Ms6.9 Milin Earthquake in the Yarlung Zangbo River Area, China. *Landslides* **2023**, *20*, 2327–2341. [CrossRef]
59. Zhang, X.; Hu, K.; Liu, S.; Nie, Y.; Han, Y. Comprehensive interpretation of the Sedongpu glacier-related mass flows in the eastern Himalayan Syntaxis. *J. Mt. Sci.* **2022**, *19*, 2469–2486. [CrossRef]

Disclaimer/Publisher's Note: The statements, opinions and data contained in all publications are solely those of the individual author(s) and contributor(s) and not of MDPI and/or the editor(s). MDPI and/or the editor(s) disclaim responsibility for any injury to people or property resulting from any ideas, methods, instructions or products referred to in the content.